

Geometric and Photometric Consistency in a Mixed Video and Galvanoscopic Scanning Laser Projection Mapping System

Petar Pjanic*

Simon Willi†

Anselm Grundhöfer‡

Disney Research

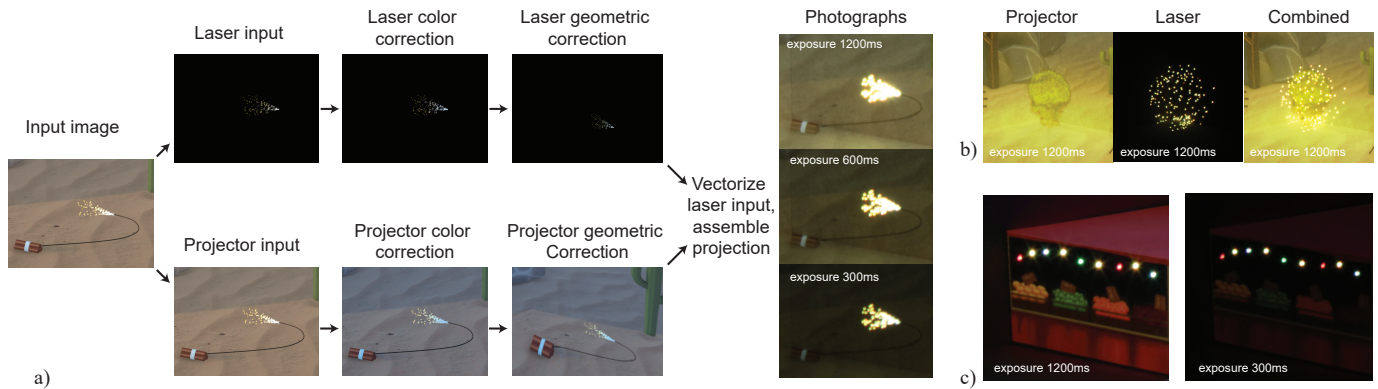


Fig. 1: (a) An input image, which is to be augmented, is separated into two representations, one for a video and one for a galvanoscopic laser projector. Both devices are geometrically and photometrically calibrated which allows to apply color corrections and geometric warping to generate consistent augmentations onto 3D geometry using both devices as can be seen in the photographs. The superimposed laser significantly increases saturation and dynamic range and enables local high dynamic range effects. In (b) and (c), photographs of additional augmented projections are shown. All photographs in the paper were taken with a Canon EOS 5D Mark II, ISO 100 and $f/22$ aperture to show consistent comparison.

Abstract—We present a geometric calibration method to accurately register a galvanoscopic scanning laser projection system (GLP) based on 2D vector input data onto an arbitrarily complex 3D-shaped projection surface. This method allows for accurate merging of 3D vertex data displayed on the laser projector with geometrically calibrated standard rasterization-based video projectors that are registered to the same geometry. Because laser projectors send out a laser light beam via galvanoscopic mirrors, a standard pinhole model calibration procedure that is normally used for pixel raster displays projecting structured light patterns, such as Gray codes, cannot be carried out directly with sufficient accuracy as the rays do not converge into a single point. To overcome the complications of accurately registering the GLP while still enabling a treatment equivalent to a standard pinhole device, an adapted version is applied to enable straightforward content generation. Besides the geometrical calibration, we also present a photometric calibration to unify the color appearance of GLPs and standard video projectors maximizing the advantages of the large color gamut of the GLP and optimizing its color appearance to smoothly fade into the significantly smaller gamut of the video projector. The proposed algorithms were evaluated on a prototypical mixed video projector and GLP projection mapping setup.

Keywords: Projector-camera systems, Calibration and registration of sensing systems, Display hardware, including 3D, stereoscopic and multi-user Entertainment, broadcast

1 INTRODUCTION AND MOTIVATION

Augmenting surfaces using projected light has become a standard technology in the entertainment industry for theme park attractions [31], ubiquitous displays [20], facade augmentations [39], gaming [18], and theatrical events [22], but it is also used to augment museum exhibits or to support industry workers. Such kind of effects are labeled in various terms such as *spatial augmented reality*, *projection*

mapping, *video mapping*, or *shader lamps*. Regardless of the term being used, such systems usually consist of one or multiple projectors and cameras that are able to process and exchange data with each other and thus are called *projector camera systems* or *procams*.

Different research fields have evolved with respect to procams. They can be roughly subdivided into the fields of manual and automatic geometric calibration and registration, radiometric and photometric adaptation and compensation, and dynamic real-time systems as well as novel 2D and 3D display systems. Several tools exist to ease the geometric calibration of multi-projector systems [1] and to apply radiometric compensation [43] to them, while dynamic systems, due to their complexity and minimal latency requirements, are currently only available as customized solutions. While procams were used to generate 3D display systems, specialized projection hardware has been developed to overcome the limitations of current projection devices in terms of contrast [15], peak brightness [9], spectral reproduction [21, 24], and frame rate [45].

This paper focuses on the issue of limited contrast and brightness and proposes a projection mapping workflow that enables the combi-

*e-mail:petar.pjanic@disneyresearch.com

†e-mail:simon@disneyresearch.com

‡e-mail:anselm@disneyresearch.com

nation of standard video projectors with GLPs to create a local high dynamic range projection. This is an extension of our earlier work focusing on the optimization of the point drawing order of GLPs [46], but with a totally different focus. Our goal here was to generate geometrically and photometrically consistent mixed video projector and GLP augmentations onto 3D geometry. To successfully accomplish this task, we present simple, but efficient workflows to achieve the required geometric and photometric mapping to accurately register the devices consistently onto the geometry.

1.1 Contribution

We propose a novel method to enhance the local contrast of projection mapping applications by providing algorithms to generate a consistent geometric and photometric registration of a mixed video and GLP mapping system. Firstly, we show how geometric calibration of a GLP can be carried out accurately using a pinhole model approximation plus an additional distortion field to seamlessly integrate such devices into standard projection mapping applications; and second, we show how the inherently different color gamuts of both devices can be analyzed and mapped such that a consistent color impression can be generated. We discuss the details of the presented algorithms, evaluate their accuracy on a prototypical hardware setup, and present a sample consistent projection mapping result that has been generated using the proposed simple and straightforward workflow.

Our work does not focus on a per-pixel photometric compensated projection, rather on a geometrically registered and photometrically mapped projection of video projectors and GLPs onto a non-textured, but potentially colored, 3D surface.

2 BACKGROUND AND RELATED WORK

The content of this paper touches different research fields, in particular calibration of procams and photometric data acquisition, color prediction, and gamut mapping. However, our work particularly focused on GLPs, which is a field of only limited research thus far. We will give a short introduction to geometric and photometric calibration, and we summarize the most relevant related literature, starting with work related to geometric calibration followed by related photometry research.

2.1 Geometric Calibration of Procams

The geometric calibration of procams consists of several components that must be estimated accurately. On the one hand, the orientation of the devices with respect to a global coordinate frame needs to be estimated. These *extrinsic* components consist of a rotation $R \in \mathbb{R}^{3 \times 3}$ and a translation $t \in \mathbb{R}^3$ that can both be combined into a joint rotation-translation transformation matrix:

$$T = [R|t] \quad (1)$$

Besides the location of the camera, the *intrinsic* properties, i.e. how the world is projected onto the device's image plane, need to be estimated as well. This is often approximated by using a pinhole model. Therefore, the focal lengths in both directions f_x and f_y as well as the location of the intersection of the optical axis with the image plane, called the principal point c_x and c_y , must be estimated. A potential skew factor can be usually neglected with modern devices. These parameters are combined into a camera matrix K .

$$K = \begin{bmatrix} f_x & 0 & c_x \\ 0 & f_y & c_y \\ 0 & 0 & 1 \end{bmatrix} \quad (2)$$

Combining the camera matrix (K) with the transformation matrix (T) into a projection matrix $P = KT$ enables projecting any homogeneous 3D world coordinate point (X, Y, Z, W) onto the according location on the device's image plane:

$$\begin{bmatrix} x \\ y \\ 1 \end{bmatrix} = P \begin{bmatrix} X \\ Y \\ Z \\ 1 \end{bmatrix} \quad (3)$$

Because optical systems have several optical flaws, such as geometric distortions, they generate images that deviate from perfect pinhole approximations. Therefore, an additional warping operation is applied to x and y to compensate for these distortion effects. Parametric models are frequently applied to correct for the usual pincushion or barrel distortion artifacts [26, 27, 38], and an undistortion function U is applied to the resulting projected 2D image plane coordinates:

$$(x_u, y_u) = U(x, y) \quad (4)$$

which ensures that the lens geometry leading to geometric deviations from a perfect pinhole approximation is corrected for.

Several methods exist to calibrate camera and projector devices using the described pinhole model, and these methods vary in several ways with respect to automation, distortion model usage as well as accuracy. Geometrically calibrating procams is an active field of research. Manual calibration methods using projections onto flat surfaces and applying the equivalent of the well-established homography-based camera calibration method by Zhang [52] are widely used [49]. However, this is not applicable in large-scale environments and is usually biased into the calibration volume, which is quite likely located in front of the real projection surface. Other recent methods have been proposed that apply a partial or even full self-calibration of procams, which largely simplifies the applicability of such systems [12, 23, 33]. All of these methods, however, assume that the devices can be described by standard pinhole models with relatively simple distortion models approximating the imperfections of optical lens systems. This is not directly applicable for GLPs because there are no lenses; instead, rotating galvanoscopic mirrors are used for image formation.

2.2 Controlling Galvanoscopic Laser Projectors

Interfacing with GLPs significantly differs from the standard communication with video projectors using display protocols such as HDMI or DisplayPort. Such systems are vector output devices and thus do not operate like standard 2D raster images. A GLP calibration for only one single-axis system was presented in [51], and another method for two axis mirror systems was shown in work by Manakov et al[30]. The authors clearly model the motion of these mirrors and describe a parametric model allowing approximation of the GLP's distorted output. This approach, however, requires a low level of control of the GLP, which makes it unsuitable for the calibration required when working with off-the-shelf GLPs as, in the latter case, no direct control of the mirrors is available – only 2D vector data can be input. Many devices use a high-level control software from Pangolin called LD2000 [36], which allows control of the GLP using a virtual 2D image plane. Although this significantly simplifies control of such devices, they are still inherently limited by the amount of content they display because the required physical mirror movements limit the potential scanning speed and thus the amount of content that can be displayed. Several approaches exist to optimize scanning to increase the amount of content that can be displayed without flickering that is caused by too slow of a scanning rate [16, 35, 37, 46]; but still, GLPs are significantly limited in the amount of displayable content.

Our work does not focus on the optimization of a specific drawing order, but rather on the ability to display content accurately at desired locations on a 3D surface, such that the GLP can be operated together with video projectors in a geometrically consistent manner. Furthermore, the color appearance of both devices should be consistent as well. The ultimate goal is the consistent superposition of video projectors with projected laser points. An extension to line drawings involves further complexity and is outside the scope of this work but will be addressed in the future (cf. Sec. 6.1 for more details).

2.3 Photometric Calibration of Procams

Accurately modeling the photometric behavior of projectors is an important research field for various procams applications. It is required to be able to compute high-quality seamless blending for multiprojection displays [28, 29, 44], but also to apply per-pixel compensated projections onto textured surfaces [2, 4, 34]. Most of the related work

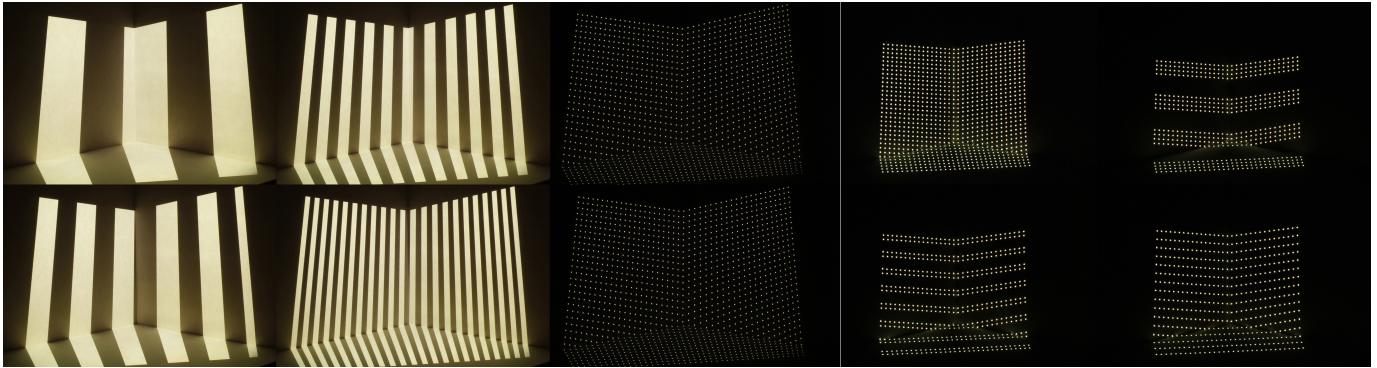


Fig. 2: Subset of the captured projected patterns used for correspondence acquisition of our prototype mockup used for evaluation: Left: Sample structured light patterns of the video projector, Gray code, and blobs, Right: Sample of the binary blobs displayed by the GLP. Note that the exposure times vary significantly between both acquisitions to avoid severe image saturation.

focuses on video projectors and, due to their limited color gamut and dynamic range, cameras are mainly used to obtain the required data for modeling the photometric behavior. If the dynamic range is not sufficient, high dynamic range images from exposure sequences of the same projection are usually used. However, when working with GLPs, monochromatic (i.e. highly saturated) colors are projected far out of the camera’s color gamut and thus cannot be accurately sensed by the image sensor. In that case, a spectral measurement device, such as a spectrophotometer is required to enable a sufficiently accurate photometric model generation.

3 WORKFLOW FOR GENERATING A CONSISTENT VIDEO AND GLP PROJECTION MAPPING SYSTEM

Achieving an accurate geometric registration as well as a consistent color appearance between a standard video projector and a GLP is challenging, as both devices are inherently different with respect to spatial image formation and color generation. In this section, we will discuss how we tried to overcome these issues and present a method to geometrically register both devices to a uniform 3D surface. We also show how the drastically varying color gamuts can be calibrated with respect to each other, thereby enabling the generation of a combined, superimposed high-contrast projection with a consistent color appearance.

3.1 Geometric Calibration

Establishing a relationship between the intrinsic properties, (e.g. lens, sensor, or laser rays), the extrinsic, (e.g. the device’s orientation in space), and the projection surface is an inevitable requirement for a high-quality projection mapping application. If the projection surface and device configuration is fully static, the main target of this step is not the estimation of a necessarily physically accurate approximation of the intrinsic calibration parameters, but to generate a transformation model that enables an accurate mapping of rendered 3D content onto the surface, the estimated intrinsic properties do not have to model the optical system realistically, but should be able to project points with the desired spatial accuracy.

The following material summarizes a geometrical calibration method that can achieve this goal. The presented approach is fully automated, does not require a specific calibration board for the calibration of video projectors and GLPs, and makes use of multiple geometrically calibrated camera devices to reconstruct the 3D projection surface. When combined with a locally nonlinear 2D displacement of the GLP’s output, a highly accurate and consistent mapping can be achieved.

3.1.1 Video Projector Calibration

As already summarized in the related work, many methods exist to calibrate standard projectors. For our calibration we applied a multi-camera-based self-calibration method to automatically carry out that

step [47]. It assumes that multiple uncalibrated cameras are observing the projection surface. In the first step these cameras will be registered automatically to a defined world coordinate space. To accomplish this task and to calibrate the video projector into that coordinate frame, binary black and white structured light patterns are projected as complementary Gray codes [8] combined with dense Gaussian blob patterns to refine the correspondences to sub-pixel accuracy (cf. to the left-hand side of Figure 2). This method can be applied in a generic setup because there are no constraints with respect to device linearity or camera orientations. Furthermore, the projected blobs are also quite insensitive in surface configurations generating a significant amount of indirect diffuse scattering. It should still be noted, however, that this structured light method is limited to operating on close to perfectly diffuse surfaces because indirect reflections, such as scattered light, caustics, and refractions, might lead to false mappings. In cases where this occurs – or other, uncontrollable light sources have been visible within the camera images – influenced areas must be masked within the captured images before processing. Because the proposed configuration also consists of a GLP, any specular surface should obviously be avoided due to safety reasons. Any static light source (e.g. exit signs) are automatically masked using a captured min and max projector illumination image and by removing all pixels without any significant change from any correspondence estimation.

Having projected the patterns, the captured camera images are processed to generate a set of sub-pixel accurate correspondences between the locations of the individual blobs on the cameras and projectors by applying an ellipse fitting method [19]. As stated before, we used multiple cameras to capture the patterns, which, after establishing the correspondences, enables the application of a multi-camera self-calibration, estimating all the device-specific T and K matrices and distortion properties, followed by a projector calibration using the method summarized in [47]. The method not only calibrates the devices individually, but also removes potential outliers generated during the structured light processing and globally optimizes all parameters using sparse bundle adjustment (SBA) [42].

3.1.2 GLP Calibration

GLPs do not display rasterized images and are only able to project a limited amount of lines and points, Gray codes cannot be displayed directly, and another strategy must be carried out to establish camera-to-GLP correspondences. Therefore, a sparse grid of regularly spaced dots were projected as a temporally binary encoded sequence to uniquely identify each point by the series of binary on/off occurrences, similar to the method presented in [53] (cf. to the right-hand side of Figure 2). Because a single laser point might shift in its spatial location, several points were drawn at each spatial position to ensure the GLP slows down the mirror sufficiently enough to create a point projection that is spatially unbiased depending on the scanning pass (the interested reader is referred to [16] and [46] for further details).

The resolution of these sparse blob patterns influences the calibration accuracy. More projected blobs means more available data, but due to the limited capabilities, the acquisition time slows down. Experiments showed that a resolution of $64 \times 64 = 4096$ points over the entire image plane of the GLP already led to an acceptable accuracy. Higher resolution is possible as well. Theoretically, each laser dot position could be used, it just takes significantly longer without a notable increase in geometric accuracy.

After image capture, the sub-pixel locations of the dot centers are detected and, after computing the GLP-to-camera correspondences for at least two of the calibrated cameras, used to reconstruct the according 3D point location on the projection surface by triangulating the projections of the laser points on the cameras' image planes. Since each laser point at a specific location is temporally encoding its ID, which can be mapped onto its unique 2D location on the rectangular virtual image plane provided by the laser projector interface, 2D-to-3D correspondences can be established using the triangulated points and can be used to calibrate the device as explained below.

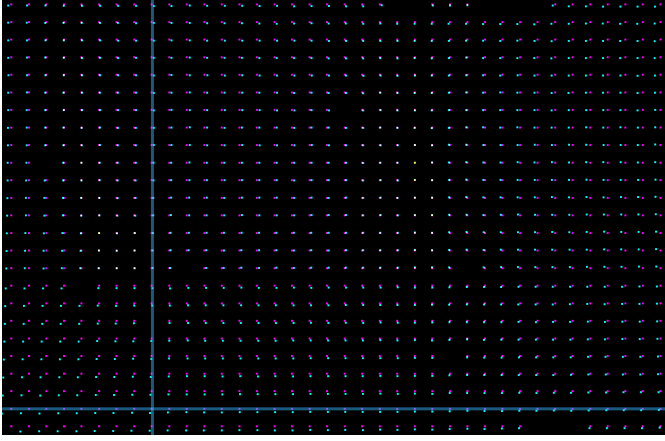


Fig. 3: Close-up of locations of the projected laser points (magenta) and calculated projections of the reconstructed 3D points using the calculated projection matrix P_{opt} (cyan). The blue bars highlight that the deviations do not follow a barrel or pincushion distortion model.

Because the GLP system has disparate distortion properties compared to an optical system – resulting from the two mirrors and their physical movement as well as the generic black box behavior of the control software being used; standard lens distortion models such as presented in [6, 17, 52] are not sufficient to accurately model these distortions. However, without taking the distortions into account, the result of the calculated perspective projection matrix components T and K will not be sufficiently accurate because the laser rays do not exactly converge into a single point and thus do not closely represent a pinhole projection. However, because the deviation from a perfect pinhole model is not drastically off, it can be used as a first, coarse model approximation, the values can be used as an initial estimate, and further nonlinear distortion can be applied to improve its accuracy. Thus, in a first calibration step, the direct linear transform algorithm [41] approach is applied using the 3D and 2D correspondences to generate a first estimate of P . This is used as an initial guess for further refinement of the approximated extrinsic and intrinsic parameters

$$P_{opt} = \arg \min_P \{F(P)\} \quad (5)$$

using a Levenberg-Marquardt optimization [32]. The cost function F is not only penalizing the distances between the expected point coordinates (c) as well as the 3D projections (pt)

$$F(P) = \sum_{i=1}^m ((P(pt_i) - c_i)^2 \dots \quad (6)$$

where m is the number of point correspondences, but it is also adding an additional error to any point that is projected outside of the image

plane:

$$\dots + \Delta(P(pt_i)) \quad (7)$$

where Δ returns the maximum distance of the point to the image plane boundary or 0 if the point hits the image plane. The latter guides the optimization to a solution for P which projects all 3D surface points back onto the image plane which is a crucial step for applying the additional 2D deformation operation and subsequently minimizing the distortion deviations.

As shown in Figure 3, the resulting projections of the reconstructed 3D coordinates are not sufficiently accurately mapping the 2D points on the image plane to the input values, leading to the requirement of an additional undistortion operation U to neutralize the deviations of the GLP from the pinhole model. Similar to the homography-based generic pre-distortion of the projection described in [50], we try to overcome the problem of an imperfectly parameterizable image distortion by applying a significantly more generic distortion function afterwards. Therefore a spline-based (or whatever smooth, nonlinear) locally varying interpolation method is applied to generate a dense distortion lookup table, warping the projected 3D points onto the right locations on the virtual image plane of the laser projector. We decided to apply a thin-plate spline interpolation [11], as this scattered data interpolator offers a smooth inter- and extrapolation of data points. Having carried out this mapping, any content that should be projected onto the projection surface area can be mapped onto the laser's image plane such that the projected laser light exactly hits the desired surface location. Therefore the polyharmonic spline function is applied as U :

$$U(pt) = \sum_{i=1}^m \omega_i \varphi(\|pt^{xy} - q_i\|) + \omega_{m+1} + \omega_{m+2} pt^x + \omega_{m+3} pt^y \quad (8)$$

where ω_i are the weighting coefficients per dimension, $\|\cdot\|$ the ℓ_2 distance, and φ the radial basis functions of the thin-plate-spline defined by:

$$\varphi(\lambda) = \begin{cases} 0, & \lambda = 0 \\ \lambda^2 \log \lambda, & \text{otherwise} \end{cases} \quad (9)$$

The individual weights ω are calculated by solving the linear system using LU decomposition as described in [10], set up using the 2D pixel correspondences between the input coordinates and the projected result using P_{opt} . Using this interpolation method, a full, dense undistortion lookup table is generated that is used to directly look up the undistorted position from arbitrary points on the virtual image plane of the laser. In a final step these distorted images are converted into a vector image representation and sent to the GLP for display.

If no full 3D mapping is required, the same pattern projection approach can also be used with at least one camera to generate a 2D mapping between camera and laser projector pixels. Instead of using a perspective projection matrix with additional 2D distortion, the densely sampled correspondences between camera pixels and laser beam positions are directly used in combination with an interpolation method to generate a dense lookup table between camera and projector pixels, as shown in [46]. This allows warping from any surface position visible on the camera image plane to the laser ray position required to illuminate that surface point. Note that 2D mapping has not been applied to the 3D mapping workflow that we are proposing here.

3.1.3 Summary

Having the video projectors as well as the GLP calibrated into the same world coordinate system enables a consistent augmentation using both devices (please refer to Section 5 for results).

The overall geometric calibration workflow of a combined video projector and GLP system consists of the following sequential steps:

1. Geometrically calibrate cameras with standard manual or self-calibration methods.
2. Calibrate video projectors using structured light projection.
3. Adjust camera exposure to capture laser dots without saturating.
4. Project binary dot patterns at specific, known 2D locations on the laser projector's virtual image plane.

5. Capture those with the cameras.
6. Process images to reveal 2D coordinates from the encoded index.
7. Reconstruct 3D positions using triangulation methods for all points that have been visible by at least two cameras.
8. Estimate the P_{opt} by using the 2D/3D correspondences.
9. Generate a dense distortion map by generating the function U using spline interpolation.

To generate a convincing seamless color augmentation, the photometric behavior of the devices must be consistently mapped as well.

3.2 Photometric Calibration

In some cases the laser projectors are not accurately photometrically calibrated, resulting in disturbing color shifts when directly projecting r, g, b values of the target colors (e.g., darker or brighter colors, hue shifts etc.). Here we present a method to photometrically calibrate the laser device to account for and correct such undesired effects.

3.2.1 Spectral Data Acquisition and Spectral Prediction Model

The proposed photometric calibration relies upon captured spectral measurements obtained with a spectrophotometer⁴. These spectral measurements $R(\lambda)$ contain the necessary information to accurately describe and characterize the reflected color.

Based on the captured spectral measurements, the next step is to create a spectral prediction model. The spectral prediction model estimates the perceived color as a spectral reflectance $R(\lambda)$ in function of the laser input r, g, b values. One approach for predicting the spectral reflectance is the application of a *black box* approach to generate a mapping between input and output color values. This implies subsampling the laser's r, g, b color space with a reasonable step width and measuring these spectral reflectance with the spectrophotometer. Then, for any r, g, b value, the corresponding spectral reflectance is calculated by accurately interpolating between the measured values. However, sometimes this approach is not practical, especially if a small step size is required to generate an accurate interpolation (i.e., for a regular step width of 10%, we need to take already $11^3 = 1331$ measurements). Depending on the non-linearity of the device, such a dense step size, or smaller, is sometimes needed.

In this paper we present a different approach by establishing a physical-based spectral prediction model. We rely on a basic principle that the outgoing reflectance of a surface, the final observed color, can be calculated by multiplying the emittance spectra of the light that illuminates that surface with the reflectance factor of that surface.

$$R(\lambda) = E(\lambda) \cdot R_f(\lambda) \quad (10)$$

where $R(\lambda)$ is the outgoing reflectance, $E(\lambda)$ is the laser spectral emittance, and $R_f(\lambda)$ is the reflectance factor of the surface. In our case, the emittance spectra is the light projected with the laser projector. The reflectance factor of the surface, if it is homogeneous, can be easily calculated by dividing the measured spectra of the projection surface with the measured spectra of the uniformly diffuse white surface such as spectralon [48, pp. 54-58].

The next step is to accurately predict the laser spectral emittance ($E(\lambda)$) for any r, g, b input values that we can provide to the laser projector. We rely on the fact that our laser projection system does not perform internal color correction or color mapping – some projection systems can perform internal color correction, which makes the spectral prediction model much more complex. This implies that the spectral emittance ($E(\lambda)$) can be calculated as a weighted sum of the red, green, and blue laser emittance at full intensity where weights are obtained by applying the response curves onto the r, g, b input values.

$$E(\lambda) = \sum_{i \in \{r, g, b\}} f_i(C_i) \cdot E_i(\lambda) \quad (11)$$

where $E(\lambda)$ is the laser spectral emittance, $E_i(\lambda)$ is the laser emittance of the red, green, and blue laser colors, and $f_i(C_i)$ is the function that applies the laser response curve to the input laser values C_i ($i \in \{r, g, b\}$).

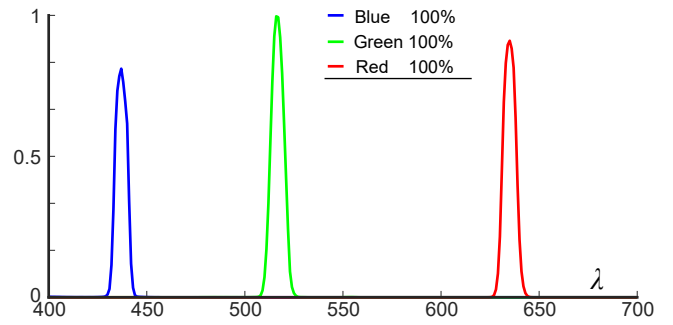


Fig. 4: Normalized laser spectral emittance for red, green and blue laser colors at full intensity.

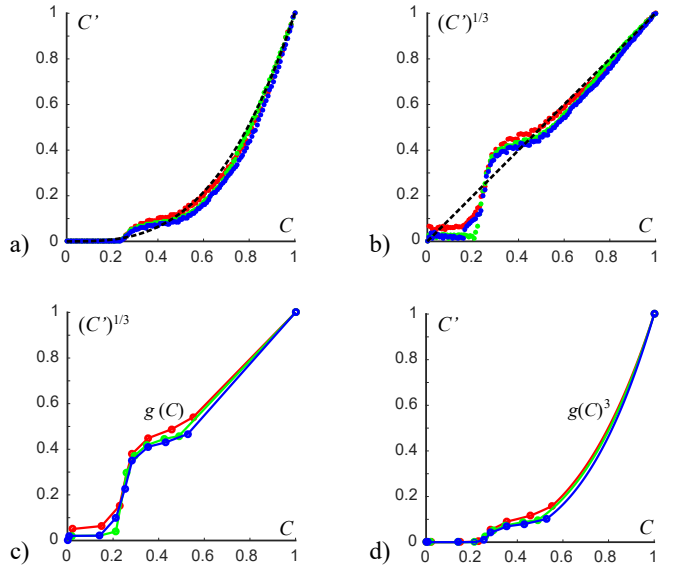


Fig. 5: Modeling the response curves for the laser projector: a) Measured responses for each of the red, green, and blue lasers, b) converting the measurements to $(C')^{1/3}$ space, c) modeling the curve in $(C')^{1/3}$ space by interpolating between selected set of points and d) converting the interpolation from $(C')^{1/3}$ to (C') space

The final part is to establish the response curve function. The response curves describe the relationship between the input values and the output intensity of the projected color. Figure 5a shows the measured response curve for a dense set of measurements. One can observe that the measurements follows an x^3 curve. This was most likely done intentionally by the manufacturer to model the nonlinear response of the human visual system[48, pp. 117-176]. However, one can observe that there are some deviations, especially in the lower part of the curve. In order to model these deviations, we first transform these values to $(C')^{1/3}$ space (Figure 5b). Then, for each r, g, b curve, we select several points and establish an interpolation function between these points (Figure 5c). Finally, the response functions are obtained by applying the inverse exponent converting the functions back to the C' space (Figure 5d).

$$f(C_i) = g_i(C_i)^3 \mid i \in \{r, g, b\} \quad (12)$$

where $f(C_i)$ is the response function, $g(C_i)$ is interpolation function in $(C')^{1/3}$ space, and C_i are input r, g, b values of the laser. The approach to establishing the interpolation curve in $(C')^{1/3}$ space allows us to accurately model the response curve with a small amount of selected points. We acknowledge that with another device the response

curve may have a drastically different shape; in that case, one can use more complex interpolation functions such as Hermite interpolation [25] to model the nonlinear response.

The following equation represents the final assembled formula describing how to predict reflectance with the proposed spectral prediction model.

$$R(\lambda) = \left(\sum_{i \in \{r, g, b\}} g_i(C_i)^3 \cdot E_i(\lambda) \right) \cdot R_f(\lambda) \quad (13)$$

where $R(\lambda)$ is outgoing reflectance, $E_i(\lambda)$ is the laser emittance of the red, green, and blue laser colors, $g_i^3(C_i)$ is the response curve function, and the C_i ($i \in \{r, g, b\}$) are the laser input values.

We applied the same photometric calibration method to the video projector as well. We are aware that this can be carried out using one of the well known camera based methods. However, since we want to generate a consistency with the GLP which cannot be accurately calibrated using cameras, a complete spectral approach without the usage of any camera device for photometric calibration simplifies the workflow for our particular task.

3.2.2 Exploring Laser Color Space and Gamut

This section explores the colors that can be achieved with the laser projector (i.e., laser color gamut), and we compare it to the colors that can be reproduced with a standard video projector². Figure 6 shows the photograph of the color pallets achieved with the laser projector using the previously established spectral prediction model. This figure shows that the laser projector is capable of reproducing the continuous mix of the red, green, and blue color primaries, thereby enabling us to cover the whole color cube without discontinuities or color artifacts.

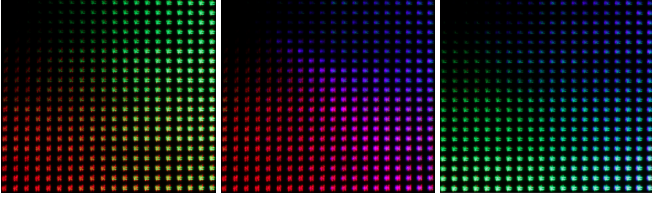


Fig. 6: The achievable laser color pallet. The photograph shows that we are able to display a continuous mix of the red, green and blue color primaries without color discontinuities or artifacts

To further detail the colors achieved with the laser projector, we used the spectral prediction model, established in Section 3.2.1 to deduce the laser color gamut in CIELAB device independent color space. The first step is to use the spectral prediction model to predict spectral reflectance for input r, g, b values by the step of 10%. Then, these spectral reflectances are converted into CIELAB color space by first converting them to the CIEXYZ space for the CIE 1931 Standard Observer [48, pp. 156-157], and then converting these CIEXYZ values to the CIELAB [48, pp. 166-168]. These points in CIELAB color space describe the shape and the volume of the laser color gamut.

Furthermore, we wanted to compare the achievable colors of the laser device to the achievable colors of the standard video projector to enhance different color areas or points. Figure 7 shows the comparison between the laser gamut (red), video projector gamut (blue), and standard sRGB gamut (dashed). One can observe that the laser gamut is much larger than what is achieved by the video projector, showing that the GLP can locally generate significantly brighter and more saturated colors compared to what the standard video projector produces.

Figure 8 further compares the differences between laser and video projectors' achievable colors. In this example we display the colors from black to full laser color (L rows), with equal steps in CIELAB space. Below these ramps are video projector ramps (P rows) that are trying to reproduce the laser color as close as possible. One can observe that at a certain point the video projector reaches its limits and is not capable of reproducing the strong and saturated colors of the laser projector. It has to be noted that the camera used to photograph

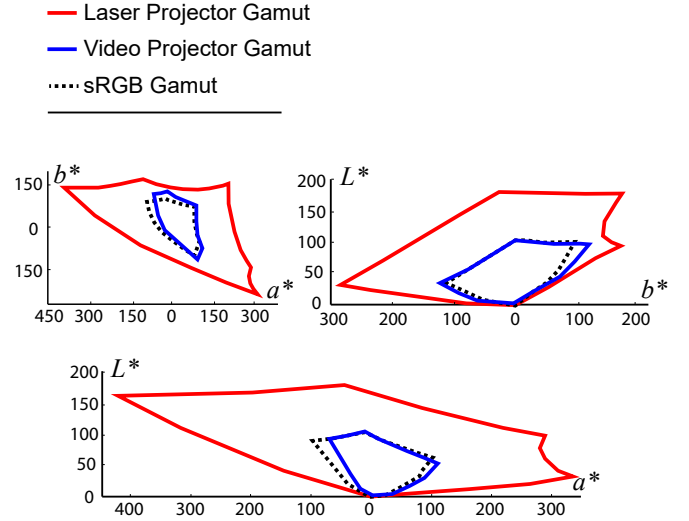


Fig. 7: The color gamuts shown in CIELAB device independent color space. The 3D color gamut volumes are shown as two dimensional projections onto CIELAB a^*b^* , L^*b^* L^*a^* axes. The red volume represents the laser projection gamut, the blue volume represents the video projector gamut and the dashed line specifies the sRGB gamut for reference. One can observe that the laser gamut is significantly larger compared to the video projector gamut.

the ramps has a limited dynamic range, which somewhat limits our ability to faithfully capture the exact differences between the laser and video projector colors.

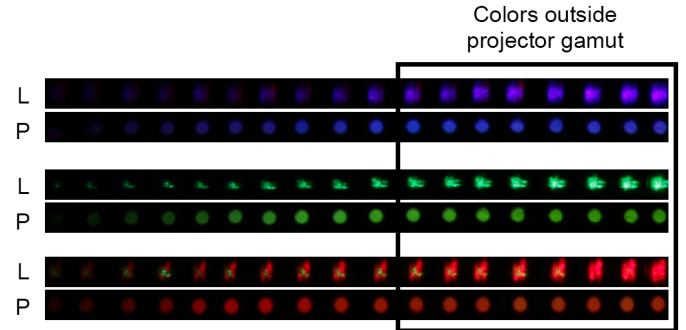


Fig. 8: Comparison between the colors of the video projector and the GLP. Ramps with L in front represent the laser color going from black to full saturation in equal steps in CIELAB color space. Ramps with P in front represents the video projector colors that are optimized to be as close as possible to the laser color. One can observe that bright colors can not be reproduced by the latter. Note that the camera gamut and dynamic range limits the ability to show the exact differences between the laser and the projector colors.

4 PROTOTYPE

The algorithms described in the last section were tested and evaluated in a real, physical projection mapping setup that will be described next.

4.1 Hardware Setup

The prototypical mixed projection-mapping system consists of six Canon DSLR cameras¹, one video projector (VP)², and a GLP³. The

¹2xCanon EOS 600D, 3xCanon EOS 1100D, Canon EOS 5D Mark II.

²Mitsubishi MH2850U.

³Semiconductor Laser Development Compact 2.7W RGB.



Fig. 9: Captured image of a sample projection mapped frame of a video sequence projected onto the three-sided mockup geometry. Upper row: Projection of the video projector alone. Lower row: Combined, geometrically, and photometrically registered projection using the video projector and GLP. Note the color hue correction as well as the significant local brightness variation. The exposure times are from left to right: 1200ms, 300ms, 75ms.

projection surface was accurately built with wood from a CAD model to be able to work with ground truth geometry data for high-quality content generation. For spectral data acquisition, a photospectrometer⁴ with a spectral resolution of $1nm$ was used. Please refer to Figure 10 for an overview.

The whole geometric calibration workflow as well as the displaying routines were realized using C++, while the color processing workflow was implemented using Matlab. A six-core Intel i7-5930K with 64 GB of RAM was used as the computing platform.

4.2 Mockup Calibration

The video projector and the cameras were automatically calibrated with respect to the projection surface using a self-calibration algorithm [47]. Therefore, structured light patterns were used as described in Section 3.1.1. Next, the GLP was geometrically calibrated as summarized in Section 3.1.2. Fiducial markers of the Aruco library [13, 14] that were integrated into the projection surface were used to transform the calibrated extrinsics of the devices into the coordinate frame of the surface in which the content was generated by the following procedure: The markers were captured by the cameras and detected in the images. Then, their 3D coordinates in the self-calibrated coordinate frame were estimated using 2D point triangulation. After this step was carried out for all markers that were visible from at least two cameras, a consistent transformation was estimated by calculating a procrustes transform [5] between the reconstructed ones and the locations of the corresponding ones in the coordinate frame of the ground truth model. This transformation was applied to the extrinsics of all devices to transform them into the world coordinate frame of the ground truth model. The fully calibrated system was then used to evaluate the algorithm’s accuracy as described in the next section.

A Spectralon was used to obtain the required radiometric measurements for estimating a photometric mapping of both devices. The spectra were measured with the photospectrometer and a mounted ND filter to avoid saturation due to the high intensity of the GLP. Results of the photometric calibration will be summarized in Section 5.2.

Figure 9 shows a sample frame of an animation of a view-dependent augmentation of the three-sided mockup. The superimposed sparkles

of the blasting fuse are significantly emphasized by the GLP projection. Because the dynamic range cannot be reproduced in that image, we have shown an exposure series.

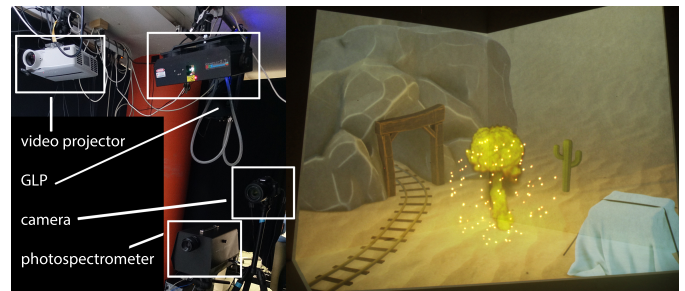


Fig. 10: Left: the hardware setup with one video projector and one GLP projecting onto the mockup. Right: A superimposed and consistently mapped view-dependent sample augmentation.

5 EVALUATION

The prototype setup helped us assess how accurately and consistently the proposed geometric calibration could register the video projector to the GLP and vice versa. Having ground truth knowledge about the 3D surface structure allowed us to carry out an accurate evaluation of the geometric calibration, which we will describe in the forthcoming section. The results of the photometric mapping are summarized as well.

5.1 Geometric Calibration Accuracy

To evaluate calibration accuracy with respect to the ground truth model, the reconstructed point clouds from the video projector as well as the GLP were compared to the planes of the ground truth geometry: each reconstructed vertex of the reconstructed point cloud was projected onto all planes of the ground truth model, and the distance to the closest plane was analyzed. The results are shown in Table 1: the average deviation is a few millimeters which resembles the limits of

⁴Photscan PR-730.

our manufacturing capabilities of the approx. $2m \times 2m$ sized projection surface.

Table 1: Distance to the ground truth CAD model in millimeters.

	avg	median	stdev	75th pctl	99.9th pctl	# pts
VP	4.117	1.713	4.626	8.941	13.112	21318
GLP	3.093	1.326	4.191	8.510	12.965	1020

To further assess how well the GLP and video projector are registered with respect to each other, the reconstructed point clouds were used and projected onto the surface by both devices. The two projections were captured by a DSLR camera⁵, and the blob centers of all 1020 3D points that were projected by both devices were compared to each other. The average deviation in camera pixels was 2.950, with a median of 2.907, which, for a camera resolution of 18 megapixels, is sufficiently accurate to be perceived as consistent by a human observer.

It should again be noted that the use of homography-based image warping as, for example, proposed in [7] will not be sufficient since it does not model any of the GLP’s distortions and thus cannot achieve the required accuracy even on planar surfaces. Furthermore, our proposed generic method enables us to create correspondences for arbitrarily shaped projection surfaces and is not limited to planar or parametric shapes.

5.2 Photometric Accuracy

Table 2 shows the prediction accuracy of the proposed spectral prediction model, for both VP and GLP, expressed as ΔE_{94} color metric. We measured the projected colors with a spectrophotometer for all combinations of input r, g, b values of 0%, 20%, 40%, 60%, 80% and 100% of maximum intensities (in total $6^3 = 216$ measurements). Then we compared the measured to predicted colors.

Table 2: This table lists the resulting ΔE_{94} color differences from the accuracy evaluation of the proposed spectral prediction model

prediction accuracy in ΔE_{94}	mean	90% quantile	max
GLP	2.01	4.20	15.85
VP	0.6	1.2	2.5

The average error for GLP is around ΔE_{94} of 2 which is quite accurate, e.g., at the level of just noticeable difference [48, pp. 168-173]. The prediction error for the VP is even smaller which is understandable taking into account that less strong and less saturated colors generate smaller errors.

Figure 11 shows that with photometric calibration we are able to create continuous intensity ramps without any loss of details.

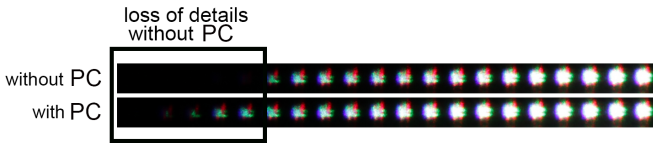


Fig. 11: The top ramp shows grey levels from black to full white without photometric calibration (without PC), i.e. the target r, g, b are directly sent to the GLP. The bottom ramp are the same grey levels generated with photometric calibration (with PC). One can observe that our approach produces more details especially in the dark areas.

Figure 12 shows the examples of reproducing color images with the GLP. The input images are shown on the left side, the images reproduced without photometric calibration are in the center and image reproduced with photometric calibration are on the right side. We can

⁵Canon EO600D

observe that our approach can produce more consistent tones and preserve more details especially in the darker areas of the image. Resolution of the images is reduced to approximately 40 by 40 pixels in order to fit the maximum number of dots that GLP can project without flickering.

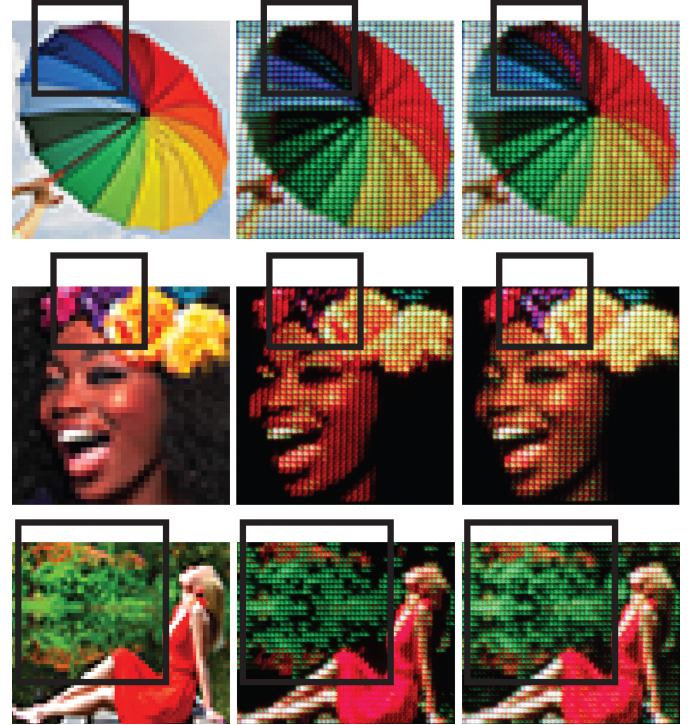


Fig. 12: The photographs showing (left) the input image that we want to display with the laser projector, (center) image projected without the photometric calibration, and (right) image produced with the proposed photometric calibration. One can observe that both approaches are capable of producing the wide range of colors however our approach preserves more details in darker areas and is capable of more accurate color reproduction.

In order to further evaluate the photometric calibration, we have conducted an informal user study where users were asked to look and evaluate the images projected with GLP. In this study, each image is projected both with and without photometric calibration. Furthermore, next to the users we placed a screen showing the original input image as a reference. We asked the users to look at both laser projected images and tell which one has more similar color-appearance to the reference image shown on the screen. For this informal user study we had 10 participants and we showed them 6 different images. The user study showed that in 81.6% of cases the users selected the image with photometric calibration to be more similar to the reference image. Furthermore, as expected based on the Figures 5 and 11, the users stated that images with photometric calibration preserve more details especially in the dark areas.

To summarize, the photometric calibration ensures a correct color reproduction of both GLP and VP. It can be used to provide an artist with more control over the final projection since it models the exact color appearance of the projected intensities. Furthermore, since the photometric calibration offers a colorimetrically accurate projection, when used as initial mapping, it has the potential to significantly speed up the necessary artist’s work to create the desired color output.

6 SUMMARY

In this paper we showed that, although the devices are inherently different, a highly accurate geometric calibration of a mixed video and GLP system can be achieved by approximating the GLP’s display properties with a pinhole projection model in combination with

a generic polyharmonic spline interpolation to model and compensate for the nonstandard distortion artifacts. This allows the straightforward content generation for such devices using 3D projection mapping applications. Furthermore, being able to accurately model the photometric properties as well as the resulting color appearance allows us to smoothly extend the limited color gamut of the video projector using the GLP's wide color gamut. We have not only presented calibration strategies to generate a consistent geometric and photometric projection mapping appearance but have also evaluated its accuracy and presented a complete sample 3D video plus GLP projection mapping workflow using a custom-built mockup.

6.1 Limitations and Future Work

Although we could show that the current approach can generate consistent projection mapping performances, the presented calibration method still limits the GLP to the projection of laser points, and their brightness is currently kept at a constant level independent of where it is projected onto the surface. Because the GLP is registered to a 3D model of the projection surface, this information can be used to extend the color calculation further to also display color-accurate line segments. In this case, the intensity must be adjusted not only according to the photometric measurements and gamut mapping operators but also to the orientation of the underlying surface geometry as this influences how fast it is traveling over the surface and thus how brightly the line will be perceived. Solving this problem and incorporating a line path optimization method into the system, similar to the ones proposed in [37] by extending the work presented in [46], is one focus of future research. During our experiments, we saw that the significant local brightness increase of the GLP leads to increased undesired indirect illumination artifacts. Compensating for them by adapting the methods presented for example in [3, 40] is another interesting research challenge to undertake.

Since our current processing pipeline requires several seconds of computation time per frame, the method cannot be directly applied to real-time systems to apply head-tracked, view dependent augmentation. Overcoming this limitation and making the system applicable for such tasks is another direction of future research.

6.2 Conclusions

Despite the fact that several display technologies such as LCDs, OLEDs, and high-resolution LED panels are currently competing against projection mapping applications, the latter still has the significant advantage of currently being the only display system that can superimpose not only close-to planar but also arbitrarily shaped surfaces. With our proposed calibration method to consistently mix different projection display devices, in particular video projectors and GLPS, we hope to stimulate additional research on how the limits of current projection-based spatial augmented reality applications can be further extended.

REFERENCES

- [1] Microsoft research. roomalive toolkit, 2017.
- [2] M. Ashdown, T. Okabe, I. Sato, and Y. Sato. Robust content-dependent photometric projector compensation. In *CVPR Workshops*, page 6. IEEE Computer Society, 2006.
- [3] O. Bimber, A. Grundhofer, T. Zeidler, D. Danch, and P. Kapakos. Compensating indirect scattering for immersive and semi-immersive projection displays. In *IEEE Virtual Reality Conference (VR 2006)*, pages 151–158, March 2006.
- [4] P.-A. Bokaris, M. Gouiffès, C. Jacquemin, and J.-M. Chomaz. Photometric compensation to dynamic surfaces in a projector-camera system. In L. Agapito, M. M. Bronstein, and C. Rother, editors, *Computer Vision - ECCV 2014 Workshops: Zurich, Switzerland, September 6-7 and 12, 2014, Proceedings, Part III*, pages 283–296, Cham, 2015. Springer International Publishing.
- [5] I. Borg and P. Groenen. *Modern Multidimensional Scaling: Theory and Applications*. Springer, 2005.
- [6] D. C. Brown. Close-range camera calibration. *Photogrammetric Engineering*, 37(8):855–866, 1971.
- [7] H. Chen, R. Sukthankar, G. Wallace, and K. Li. Scalable alignment of large-format multi-projector displays using camera homography trees. In *IEEE Visualization*, pages 339–346, Nov 2002.
- [8] O. Choi, H. Lim, and S. C. Ahn. Robust binarization of gray-coded pattern images for smart projectors. In *International Conference on Electronics, Information, and Communications (ICEIC)*, pages 1–4, Jan 2016.
- [9] G. Damberg, A. Ballestad, E. Kozak, R. Kumaran, and J. Minor. Efficient, high brightness, high dynamic range projection. In *ACM SIGGRAPH 2014 Emerging Technologies*, pages 18:1–18:1, New York, NY, USA, 2014. ACM.
- [10] G. Donato and S. Belongie. Approximate thin plate spline mappings. In *Proceedings of the 7th European Conference on Computer Vision-Part III, ECCV '02*, pages 21–31, London, UK, UK, 2002. Springer-Verlag.
- [11] J. Duchon. Splines minimizing rotation-invariant semi-norms in sobolev spaces. In W. Schempp and K. Zeller, editors, *Constructive Theory of Functions of Several Variables: Proceedings of a Conference Held at Oberwolfach April 25 – May 1, 1976*, pages 85–100, Berlin, Heidelberg, 1977. Springer Berlin Heidelberg.
- [12] S. Garrido-Jurado, R. Muñoz-Salinas, F. Madrid-Cuevas, and M. Marn-Jiménez. Simultaneous reconstruction and calibration for multi-view structured light scanning. *Journal of Visual Communication and Image Representation*, 39:120 – 131, 2016.
- [13] S. Garrido-Jurado, R. M. noz Salinas, F. Madrid-Cuevas, and M. Marín-Jiménez. Automatic generation and detection of highly reliable fiducial markers under occlusion. *Pattern Recognition*, 47(6):2280 – 2292, 2014.
- [14] S. Garrido-Jurado, R. M. noz Salinas, F. Madrid-Cuevas, and R. Medina-Carnicer. Generation of fiducial marker dictionaries using mixed integer linear programming. *Pattern Recognition*, 51:481 – 491, 2016.
- [15] M. Gibbon, S. Zhou, S. Adkins, S. Anikichev, G. Moss, and B. Eckersley. Equipment and techniques for increasing the dynamic range of a projection system, May 23 2006. US Patent 7,050,122.
- [16] O. Halabi and N. Chiba. Efficient vector-oriented graphic drawing method for laser-scanned display. *Displays*, 30(3):97 – 106, 2009.
- [17] J. Heikkilä and O. Silven. A four-step camera calibration procedure with implicit image correction. In *Proceedings of IEEE Computer Society Conference on Computer Vision and Pattern Recognition*, pages 1106–1112, Jun 1997.
- [18] B. R. Jones, H. Benko, E. Ofek, and A. D. Wilson. Illumiroom: Immersive experiences beyond the tv screen. In *Communications of the ACM*, volume 58, pages 93–100, New York, NY, USA, May 2015. ACM.
- [19] K. Kanatani, Y. Sugaya, and Y. Kanazawa. *Ellipse Fitting for Computer Vision: Implementation and Applications*. Synthesis Lectures on Computer Vision. Morgan & Claypool Publishers, 2016.
- [20] M. Kasetani, T. Noguchi, H. Yamazoe, and J. H. Lee. Projection mapping by mobile projector robot. In *12th International Conference on Ubiquitous Robots and Ambient Intelligence (URAI)*, pages 13–17, Oct 2015.
- [21] I. Kauvar, S. J. Yang, L. Shi, I. McDowall, and G. Wetzstein. Adaptive color display via perceptually-driven factored spectral projection. In *ACM Transactions on Graphics*, volume 34, pages 165:1–165:10, New York, NY, USA, Oct. 2015. ACM.
- [22] J. Lee, Y. Kim, M.-H. Heo, D. Kim, and B.-S. Shin. Real-time projection-based augmented reality system for dynamic objects in the performing arts. In *Symmetry*, volume 7, pages 182–192, 2015.
- [23] F. Li, H. Sekkati, J. Deglint, C. Scharfenberger, M. Lamm, D. Clausi, J. Zelek, and A. Wong. Simultaneous projector-camera self-calibration for three-dimensional reconstruction and projection mapping. *IEEE Transactions on Computational Imaging*, 3(1):74–83, March 2017.
- [24] Y. Li, A. Majumder, D. Lu, and M. Gopi. Content-independent multi-spectral display using superimposed projections. In *Computer Graphics Forum*, volume 34, pages 337–348, Chichester, UK, May 2015. The Eurographics Association; John Wiley and Sons, Ltd.
- [25] R. Lorentz. Multivariate hermite interpolation by algebraic polynomials: A survey. *Journal of Computational and Applied Mathematics*, 122(12):167 – 201, 2000. Numerical Analysis in the 20th Century Vol. II: Interpolation and Extrapolation.
- [26] L. Ma, Y. Chen, and K. L. Moore. A family of simplified geometric distortion models for camera calibration. *CoRR*, cs.CV/0308003, 2003.
- [27] L. Ma, Y. Chen, and K. L. Moore. Rational radial distortion models with analytical undistortion formulae. *CoRR*, cs.CV/0307047, 2003.
- [28] A. Majumder and R. Stevens. Lam: Luminance attenuation map for photometric uniformity in projection based displays. In *Proceedings of the ACM Symposium on Virtual Reality Software and Technology, VRST '02*, pages 147–154, New York, NY, USA, 2002. ACM.

- [29] A. Majumder and R. Stevens. Perceptual photometric seamlessness in projection-based tiled displays. In *ACM Transactions on Graphics*, volume 24, pages 118–139, New York, NY, USA, Jan. 2005. ACM.
- [30] A. Manakov, H.-P. Seidel, and I. Ihrke. A mathematical model and calibration procedure for galvanometric laser scanning systems. *16th International Workshop on Vision, Modeling and Visualization*, pages 207–214, 2011.
- [31] M. R. Mine, J. van Baar, A. Grundhfer, D. Rose, and B. Yang. Projection-based augmented reality in disney theme parks. *IEEE Computer*, 45(7):32–40, 2012.
- [32] J. J. Moré. The Levenberg-Marquardt algorithm: Implementation and theory. In G. A. Watson, editor, *Numerical Analysis*, pages 105–116. Springer, Berlin, 1977.
- [33] D. Moreno and G. Taubin. Simple, accurate, and robust projector-camera calibration. In *Proceedings of the 2012 Second International Conference on 3D Imaging, Modeling, Processing, Visualization & Transmission*, 3DIMPVT '12, pages 464–471, Washington, DC, USA, 2012. IEEE Computer Society.
- [34] S. K. Nayar, H. Peri, M. D. Grossberg, and P. N. Belhumeur. A projection system with radiometric compensation for screen imperfections. In *First IEEE International Workshop on Projector-Camera Systems (PRO-CAMS)*, 2003.
- [35] Pangolin. Pangolin laser systems lasershow converter max. http://www.pangolin.com/LD2000/lc-max_overview.htm.
- [36] Pangolin. Pangolin laser systems ld 2000. http://www.pangolin.com/LD2000/LD2000_sdk.htm.
- [37] A. Purkhet, O. Halabi, T. Fujimoto, and N. Chiba. Accurate and efficient drawing method for laser projection. *The Journal of the Society for Art and Science*, 7(4):155–169, 2008.
- [38] C. Ricolfè-Viala and A.-J. Sanchez-Salmeron. Lens distortion models evaluation. In *Applied Optics*, volume 49, pages 5914–5928. OSA, Oct 2010.
- [39] D. Rossi. Smart architectural models: Spatial projection-based augmented mock-up. In *Digital Heritage International Congress (Digital Heritage)*, volume 2, pages 677–684, Oct 2013.
- [40] Y. Sheng, T. C. Yapo, and B. Cutler. Global Illumination Compensation for Spatially Augmented Reality. In *Computer Graphics Forum*. The Eurographics Association and Blackwell Publishing Ltd, 2010.
- [41] I. E. Sutherland. Three-dimensional data input by tablet. In *ACH SIG-GRAPH*, volume 8, pages 86–86, New York, NY, USA, Sept. 1974. ACM.
- [42] B. Triggs, P. F. McLauchlan, R. I. Hartley, and A. W. Fitzgibbon. Bundle adjustment - a modern synthesis. In *Proceedings of the International Workshop on Vision Algorithms: Theory and Practice, ICCV '99*, pages 298–372, London, UK, UK, 2000. Springer-Verlag.
- [43] Vioso. Autoalignment, 2017.
- [44] G. Wallace, H. Chen, and K. Li. Color gamut matching for tiled display walls. In *Proceedings of the Workshop on Virtual Environments, EGVE '03*, pages 293–302, New York, NY, USA, 2003. ACM.
- [45] Y. Watanabe, G. Narita, S. Tatsuno, T. Yuasa, K. Sumino, and M. Ishikawa. High-speed 8-bit image projector at 1,000 fps with 3 ms delay. *The International Display Workshops*, pages 1064–1065, 2015.
- [46] S. Willi and A. Grundhöfer. Spatio-temporal point path analysis and optimization of a galvanoscopic scanning laser projector. *IEEE Transactions on Visualization and Computer Graphics*, 22(11):2377–2384, 2016.
- [47] S. Willi and A. Grundhöfer. Robust geometric self-calibration of generic multi-projector camera systems. *IEEE International Symposium on Mixed and Augmented Reality (ISMAR)*, 2017.
- [48] G. Wyszecki and W. S. Stiles. *Color science : concepts and methods, quantitative data and formulae*. The Wiley series in pure and applied optics. Wiley, New York, 1982. A Wiley-Interscience publication.
- [49] L. Yang, J. M. Normand, and G. Moreau. Practical and precise projector-camera calibration. In *IEEE International Symposium on Mixed and Augmented Reality (ISMAR)*, pages 63–70, Sept 2016.
- [50] S. Yang, M. Liu, J. Song, S. Yin, Y. Guo, Y. Ren, and J. Zhu. Flexible digital projector calibration method based on per-pixel distortion measurement and correction. *Optics and Lasers in Engineering*, 92:29 – 38, 2017.
- [51] C. Yu, X. Chen, and J. Xi. Modeling and calibration of a novel one-mirror galvanometric laser scanner. *Sensors*, 17(1), 2017.
- [52] Z. Zhang. A flexible new technique for camera calibration. *IEEE Transactions on Pattern Analysis and Machine Intelligence*, 22(11):1330–1334, Nov. 2000.
- [53] S. Zollmann, T. Langlotz, and O. Bimber. Passive-active geometric calibration for view-dependent projections onto arbitrary surfaces. *JVRB - Journal of Virtual Reality and Broadcasting*, 4(2007)(6), 2007.